

# Optomechanical platform for high-frequency gravitational wave and vector dark matter detection

David Roussel,\* Moritz Bjoern Kristiansson Kunze,† and Christoph Reinhardt‡

Deutsches Elektronen-Synchrotron DESY, 22603 Hamburg, Germany

(Dated: January 7, 2026)

We present a proposal for a nanomechanical membrane resonator integrated into a moderate-finesse ( $\mathcal{F} \sim 10$ ) optical cavity as a versatile platform for detecting high-frequency gravitational waves and vector dark matter. Gravitational-wave sensitivity arises from cavity-length modulation, which resonantly drives membrane motion via the radiation-pressure force. This force also enables *in situ* tuning of the membrane's resonance frequency by nearly a factor of two, allowing a frequency coverage from 0.5 to 40 kHz using six membranes. The detector achieves a peak strain sensitivity of  $2 \times 10^{-23}/\sqrt{\text{Hz}}$  at 40 kHz. Using a silicon membrane positioned near a gallium-arsenide input mirror additionally provides sensitivity to vector dark matter via differential acceleration from their differing atomic-to-mass number ratios. The projected reach surpasses the existing limits in the range of  $2 \times 10^{-12}$  to  $2 \times 10^{-10}$  eV/c<sup>2</sup> for a one-year measurement. Consequently, the proposed detector offers a unified approach to searching for physics beyond the Standard Model, probing both high-frequency gravitational waves and vector dark matter.

## I. INTRODUCTION AND DETECTOR CONCEPT

Ten years since the advent of gravitational wave (GW) detection [1], the LIGO, Virgo, and KAGRA observatories have transformed astrophysics, enabling new tests of general relativity and a deeper understanding of black holes and neutron stars [2]. These kilometer-scale interferometers are optimized for frequencies up to a few kHz, as their sensitivity towards higher frequencies is ultimately limited by shot noise [3, 4]. Toward the upper end of their observational band, particularly in the 700–1500 Hz range, an especially enticing target are continuous GW signals generated by deformations of rapidly rotating neutron stars, which can probe the equation of state of ultra-dense matter and help explain the observed paucity of fast pulsars [5]. Furthermore, several beyond-Standard-Model (BSM) scenarios predict GW signals at higher frequencies, extending beyond the kHz-range, including those from primordial black hole mergers, axion superradiance, cosmic strings, and early-universe phase transitions [6, 7]. This has fueled the development of novel high-frequency gravitational wave (HFGW) detectors that circumvent the limitations of the large-scale laser observatories [6, 8].

Devised approaches include detectors based on superconducting cavities [9, 10], circuits [11], and magnets [12]; broadband electromagnetic detectors [13], probes of the frequency or polarization of laser light [14, 15]; bulk acoustic wave resonators [16, 17], and superfluid helium [18]. Another concept is the levitated sensor detector (LSD), in which the mechanical resonance of an optically-levitated nanodisk inside a 100-m optical cavity transduces the GW strain into an optical signal [19, 20].

While theoretical sensitivity to BSM signatures has been demonstrated, the LSD faces significant technical challenges: maintaining stable levitation of a high-aspect-ratio particle in ultra-high vacuum, and the need for a cavity mirror of unprecedented radius  $\sim 1$  m to suppress scattering at the nanodisk.

Here we propose a complementary platform in which the levitated disk is replaced by an optically trapped nanomechanical membrane resonator [21–23]. Membranes with millimeter-scale lateral dimensions are readily fabricated [24, 25] and can be stably integrated into an optical cavity via their supporting chip [26, 27], thereby eliminating the two major technical barriers of the LSD.

A distinctive feature of our design is its dual sensitivity. In addition to HFGWs, the detector can probe certain models of vector dark matter (VDM), a light spin-1 dark-sector candidate such as the dark photon [28–30]. In our setup, sensitivity arises from the baryon-lepton number (B-L) coupling between the silicon membrane and the gallium arsenide input mirror, which is reflected in these materials' distinct neutron-to-nucleon ratios [31, 32]. Projected sensitivities show competitive reach with the LSD for HFGWs [20] and surpass existing bounds from the Eöt-Wash experiment as well as LIGO/Virgo for VDM, in the kHz band [33, 34].

Thus, the proposed optomechanical platform simultaneously targets both gravitational waves and B-L coupled vector dark matter, offering a unified experimental approach to physics beyond the Standard Model.

Figure 1(a) illustrates the underlying concept of the optomechanical detector platform. A nanomechanical membrane is placed near the input mirror inside a hemispherical optical cavity of length  $L = 100$  m, thereby forming a membrane-at-the-edge optomechanical system [35]. A Michelson configuration of two such cavities is considered to suppress noise common to both arms. Examples include vibrations, laser intensity fluctuations, or frequency noise, which couple to the gravitational-wave readout as sidebands on the laser carrier frequency. How-

\* david.roussel@cern.ch

† moritz.kunze@online.de

‡ christoph.reinhardt@desy.de

ever, in a symmetric Michelson interferometer, common-mode rejection ensures these sidebands are reflected back to the input port and do not affect the detection port [3].

The membrane is trapped at an antinode of an optical field (red), which tunes its effective resonance frequency as [22]:

$$\Omega_{\text{eff}} = \sqrt{\Omega_m^2 + k_{\text{opt}}/m_{\text{eff}}}. \quad (1)$$

Here,  $\Omega_m/2\pi$  and  $m_{\text{eff}}$  are the membrane's resonance frequency and effective mass, while  $k_{\text{opt}} = (16\pi/\lambda)(|r|/|t|)(\mathcal{P}_{\text{trap}}/c)$  denotes the optical spring constant, with  $\lambda$  and  $\mathcal{P}_{\text{trap}}$  the trapping field wavelength and power, and  $r$  and  $t$  the membrane's reflection and transmission coefficients [36].

A passing GW of frequency  $\omega_{\text{GW}}/2\pi$  modulates the cavity length  $L$ , displacing the antinode of the trapping field relative to the membrane by  $x$  [19, 20]. This force resonantly excites the membrane when  $\omega_{\text{GW}} = \Omega_{\text{eff}}$ .

Choosing gallium arsenide (GaAs) for the input mirror's material not only enables low-loss injection of laser light [37–39], but also provides sensitivity to VDM. This sensitivity arises from the difference in neutron-to-nucleon ratios between the GaAs input mirror and the silicon (Si) membrane,  $\Delta_{12} = Z_{\text{GaAs}}/A_{\text{GaAs}} - Z_{\text{Si}}/A_{\text{Si}} = 0.05$ . For a membrane-mirror separation much smaller than the de Broglie wavelength corresponding to the mass of the VDM, the oscillating VDM field effectively exerts a spatially uniform differential acceleration  $a \propto \Delta_{12}$  between them, which, analogous to the GW case, is resonantly enhanced when the VDM oscillation frequency matches the membrane resonance,  $\omega_{\text{DM}} = \Omega_{\text{eff}}$  [25, 30, 32].

For the membrane geometry, trampolines [40, 41] with branched tethers [42] are considered, as shown in Fig. 1(b), since they offer among the highest  $Q$  values and wide frequency tunability when optically trapped. The first and second symmetric modes, denoted  $s1$  and  $s2$ , are shown in the upper and lower panels, respectively.

## II. MODEL SETUP

A main objective of the detector design is to minimize the ratio

$$\sqrt{S_F}/m_{\text{eff}}, \quad (2)$$

as both HFGW (Eq. 6) [19, 20] and VDM (Eq. 7) [30, 32] sensitivities scale proportionally with it. Here,

$$S_F = 4k_B T m_{\text{eff}} \gamma_{\text{tot}}, \quad (3)$$

is thermal force noise power spectral density [44], where  $T$  is the temperature, and the membrane's total mechanical damping rate [19, 20],

$$\gamma_{\text{tot}} = \gamma_g + \gamma_{\text{sc}}/N_i + \gamma_m, \quad (4)$$

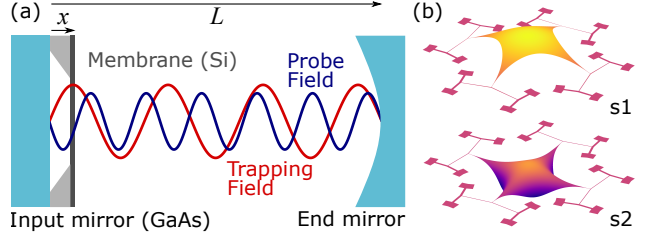


FIG. 1. Schematic of the optomechanical detector platform. (a) A nanomechanical silicon (Si) membrane (gray) is positioned near the gallium arsenide (GaAs) input mirror inside an optical cavity of length  $L$ . The membrane's equilibrium position coincides with an antinode of an optical trapping field (red) with power  $\mathcal{P}_{\text{trap}}$ , which tunes the membrane's resonance frequency  $\Omega_{\text{eff}}(\mathcal{P}_{\text{trap}})/2\pi$ . A passing gravitational wave at this frequency resonantly excites the membrane to oscillate with amplitude  $x$ , which is measured via a probe field (blue). The combination of the GaAs input mirror and Si membrane allows simultaneous sensitivity to vector dark matter models, due to both materials' distinct baryon and lepton number. Only one optomechanical cavity is shown; the full detector uses two in a Michelson configuration to suppress technical noise. (b) The mode shapes of the first and second symmetric modes, denoted  $s1$  (upper) and  $s2$  (lower) respectively, simulated with COMSOL Multiphysics [43], of an ultra-high-Q trampoline membrane featuring branched tethers.

is constituted by contributions from residual gas  $\gamma_g$ , scattering photons  $\gamma_{\text{sc}}$ , and intrinsic mechanical loss  $\gamma_m$ .  $N_i = k_B T / \hbar \Omega_{\text{eff}}$  is the mean initial phonon occupation number of the centre-of-mass motion.

The gas damping rate is given by  $\gamma_g = (P/\rho d) \sqrt{32M_{\text{gas}}/\pi RT}$  [45], with molar mass of the residual gas  $M_{\text{gas}}$ , and the mass density  $\rho$  and thickness  $d$  of the membrane.

Photons scattering of the membrane contribute with a damping rate  $\gamma_{\text{sc}} = \lambda \Omega_{\text{eff}} / [16(n^2 - 1)d \mathcal{F}_{\text{mem}}] (w/a)^2$  [19, 20], where  $\Omega_{\text{eff}}$  is given by Eq. 1,  $n$  is the refractive index of the membrane material, and  $\mathcal{F}_{\text{mem}}$  is the membrane-limited cavity finesse, which depends on the scattering of cavity light at the membrane. The ratio  $w/a$  is the beam-waist-to-pad-radius ratio of the optical mode on the membrane. As the membrane pad is not circular, the pad-radius is conservatively taken to be the radius of the largest circle that fits within the membrane pad (see Fig. 1(b)). The laser beam waist on the membrane is constrained on the lower end by practical mirror diameter and on the upper end by scattering losses at the membrane. We consider  $w \gtrsim 375 \mu\text{m}$ , compatible with an end mirror radius of 0.2 m, such as used in LIGO [46].  $\mathcal{F}_{\text{mem}}$  depends sensitively on the ratio of beam waist to membrane pad radius,  $w/a$  [21]. Scattering increases rapidly for  $w/a \gtrsim 0.6$ , while smaller ratios distort the mechanical mode and reduce  $Q$  [22, 47]. The optimal ratio is therefore fixed at  $w/a = 0.6$ , corresponding to  $\mathcal{F}_{\text{mem}} \approx 5.5 \times 10^3$  [21]. This constraint also sets the smallest achievable pad size and thus the highest operational frequency for the considered membrane geometry.

The intrinsic mechanical dissipation is given by  $\gamma_m = \Omega_{\text{eff}}/Q$ , where  $Q$  is the mechanical quality-factor of the membrane at the resonance frequency. The quality factor is calculated from COMSOL simulations as  $Q = 2\pi W/\Delta W$  [22, 47–49], where  $W = \Omega_{\text{eff}}^2 \rho d \iint u^2 dA/2$  is the energy stored in the mode of normalized shape  $u = u(x, y)$ .  $\Delta W = \pi Y d^3 / [12(1 - \nu^2) Q_{\text{int}}] \iint \xi(x, y) dA$  is the mode's bending-related energy loss, with Young's modulus  $Y$ , Poisson ratio  $\nu$ , intrinsic material quality factor  $Q_{\text{int}}$ , where  $\xi(x, y)$  is given by [48]

$$\xi(x, y) = \left( \frac{\partial^2 u}{\partial x^2} + \frac{\partial^2 u}{\partial y^2} \right)^2 - 2(1 - \nu) \left[ \frac{\partial^2 u}{\partial x^2} \frac{\partial^2 u}{\partial y^2} - \left( \frac{\partial^2 u}{\partial x \partial y} \right)^2 \right]. \quad (5)$$

The effective mass of the fundamental mode is determined from finite-element simulations as  $m_{\text{eff}} = \rho t \iint u(x, y)^2 dA / \max[u(x, y)^2]$ . All simulations were performed using the *Shell* interface in the *Structural Mechanics* module of COMSOL Multiphysics (v6.2) [43].

The setup is engineered to minimize the contributing damping mechanisms through appropriate choice of materials, geometry, and environmental parameters.

### A. Operating Environment

To suppress thermal noise (Eq. 3) and gas-damping, we assume the setup is situated inside an ultra-high-vacuum cryostat at  $P = 10^{-11}$  mbar and  $T = 4$  K. At this pressure, hydrogen is the dominant residual gas species [50, 51].

### B. Membrane Geometry and Material Parameters

The membrane material is crystalline silicon (Si), chosen for its ultra-low optical and mechanical loss [52, 53] and high thermal conductivity at cryogenic temperatures [54, 55], which efficiently dissipates heat from residual optical absorption, as confirmed with COMSOL simulations. In our simulations, we use the material parameters of crystalline silicon, summarized in Table I. Assuming surface loss to be the dominant dissipation channel [52, 56, 57], the intrinsic quality factor is scaled linearly with membrane thickness  $d$  as  $Q_{\text{int}} = 3.5 \times 10^5 d / 120 \text{ nm}$ , which is consistent with measurements from oxide-free membranes [52].

The aspects of the membrane design such as overall extent, pad size, thickness, and internal stress were designed via parameter sweeps to yield the best sensitivity at different resonant frequencies. The pad size is limited on the lower end by the minimum value for the membrane-limited cavity finesse  $\mathcal{F}_{\text{mem}}$  as described above. The pad size is also limited on the upper end geometrically with respect to the membrane's overall extent and the branched supporting tethers. The overall lateral dimensions are limited to  $8 \times 8 \text{ cm}^2$ , for compatibility with the fabrication on a four-inch diameter wafer.

### C. Optical Cavity Response

The operating wavelength is 1550 nm, providing minuscule optical loss both in the silicon membrane and the gallium-arsenide (GaAs) cavity input mirror [37–39]. The silicon membrane is positioned near the cavity input mirror within an optical cavity of length  $L = 100$  m and finesse  $\mathcal{F}_{\text{cav}} = 10$ . This configuration forms a membrane-at-the-edge optomechanical system in which the membrane's equilibrium position coincides with an antinode of the optical trapping field. We define  $H(\Omega) = \sqrt{1 + (2\mathcal{F}_{\text{cav}}/\pi)^2 \sin^2(\Omega L/c)}$  as the cavity response function [19, 20].

### D. Considered Best-Case Membrane Designs

The membrane designs for the considered *best-case scenario* are assuming a membrane thickness of 500 nm, which is consistent with the commonly available upper limit for the device layer thickness of silicon-on-insulator wafers. Furthermore, an internal stress at the theoretical strength limit of 20 GPa for silicon [61] is considered. In terms of membrane designs, starting from the lowest frequency, this corresponds to the membrane with the largest extent and pad size. It was determined that for the considered s1 and s2 membrane modes [see Fig. 1(b)], the best sensitivity was achieved by keeping the overall extent of the membrane fixed, while increasing the stress to increase the resonant frequency. When doing so was no longer possible, the stress was also kept fixed while either the pad size or the membrane extent was reduced to increase the resonant frequency. The uppermost frequency is obtained for  $w/a$  fixed at 0.6.

TABLE I. Baseline parameters used in simulations. Material constants are for crystalline silicon, where values given in parentheses represent the limiting best-case scenario.

Parameter	Symbol	Value
Young's modulus [57]	$Y$	169 GPa
Mass density [57]	$\rho$	2330 kg/m <sup>3</sup>
Poisson ratio [58]	$\nu$	0.278
Refractive index (1550 nm) [59]	$n$	3.45
Thickness	$d$	100 nm (500 nm)
Internal stress	$\sigma$	1.5–3 GPa (20 GPa)
Temperature	$T$	4 K
Gas pressure (H <sub>2</sub> )	$P$	$10^{-11}$ torr
Molar mass (H <sub>2</sub> ) [60]	$M_{\text{gas}}$	2.016 g/mol
Cavity length	$L$	100 m
Cavity finesse	$\mathcal{F}_{\text{cav}}$	10
Laser wavelength	$\lambda$	1550 nm
Membrane-limited finesse	$\mathcal{F}_{\text{mem}}$	$5.5 \times 10^3$
Beam waist to pad radius ratio	$w/a$	0.6

### E. Optically-Tuned Membrane Designs

With regard to a first practical implementation of our detector concept, we consider six specific membrane designs with a thickness of 100 nm and an optical trapping power up to 20 W. Regarding already demonstrated devices [57], we initially set the stress at 1.5 GPa. The lowest resonance frequency is obtained for the largest membrane extent and pad size, as for the best case scenario (previous sub-section). It was determined that the best sensitivity was achieved by keeping the overall size of the membrane fixed, while only reducing the pad size to increase the resonant frequency. After doing so for five membranes, the limit  $w/a \sim 0.6$  is reached. Further increasing the membrane's intrinsic resonance frequency, is realized by increasing the stress to 3 GPa. These high stresses may be achieved with strain engineering the membrane's supporting structure [62]. As presented in the following sections, the resulting frequency coverage of the six membranes is 0.5 to 40 kHz. When increasing the optical trapping power applied to a membrane, the increase in resonance frequency eventually reaches a plateau. For the s1 mode of the trampoline membranes, this occurs around twice the original resonant frequency. Thus, at a laser power of 20 W one can reach a frequency that is about 1.5-1.9 times the intrinsic resonance frequency. The s2 mode's frequency increases by about 1.03-1.06 times the intrinsic resonance frequency, at 20 W laser power.

### III. SENSITIVITY TO HIGH FREQUENCY GRAVITATIONAL WAVES

The strain sensitivity  $h_{\min}$  at the membrane's resonance frequency  $\omega_{\text{GW}} = \Omega_{\text{eff}}$  is given by the following equation [19, 20]:

$$h_{\min} = \frac{2}{\omega_{\text{GW}}^2 L} \frac{\sqrt{S_F}}{m_{\text{eff}}} H(\omega_{\text{GW}}), \quad (6)$$

where  $S_F$  is given by Eq. 3.

Figure 2a shows the sensitivity for the considered best-case scenario (see Sec. II D), with the dark and light blue traces corresponding to the s1 and s2 modes, respectively. The red traces represent the six specific optically tuned membrane designs, showing how the resonance frequency and sensitivity changes as the laser power is varied between 1 to 20 W. The minimum strain to which aLIGO is sensitive is shown in grey [63], which can be seen to be increasing with frequency due to the shot noise limitation until it no longer has sensitivity. This contrasts with the membrane-based setup whose minimum sensitive strain decreases with frequency due to the underlying principle of resonant force detection.

Figure 2b shows the contribution of the gas damping, photon scattering, mechanical loss, and effective mass to the sensitivity of the best-case scenario. It is evident that

for the s1 mode, gas damping is, for the most part, the dominant loss mechanism and, hence, the limiting factor for sensitivity, whereas photon scattering is of least concern. The discontinuity arises when the sensitivity changes from maintaining the maximum pad size with a reducing membrane extent to maintaining the maximum membrane extent with a reducing pad size. However, for the s2 mode, the mechanical loss begins to dominate due to a reduced  $Q$ -factor, and the photon-scattering becomes more important than gas-damping due to its frequency-dependence.

Figure 2c shows the corresponding contributions of the various loss mechanisms and the effective mass of the six optically-tuned membrane designs. The worsening of the sensitivity of a specific membrane design with increasing laser power can be seen to arise primarily due to the  $Q$ -factor of the membrane decreasing with laser power. This is due to the beam waist needing to be much smaller than the pad (see Sec. II), to suppress scattering loss, which significantly affects the mode shape, and therefore the bending-loss limited  $Q$ -factor [22, 47]. However, if one was not restricted by this consideration, having a larger waist would result in a more even laser beam profile over the pad, and in the six specific membrane designs therefore an even higher  $Q$ -factor.

### IV. SENSITIVITY TO VECTOR DARK MATTER

The peak sensitivity to a given dark matter mass  $m_{\text{DM}} = \omega_{\text{DM}} \hbar / c^2$  occurs when the resonance frequency of the membrane matches the frequency  $f_{\text{DM}} = \omega_{\text{DM}} / 2\pi$ . The minimum coupling  $g_{\min}$  one would be sensitive to, averaged over the possible polarizations, is given by [30, 32]:

$$g_{\min} = \frac{\sqrt{3/2}}{\beta \Delta_{12} a_0} \sqrt{\frac{\omega_{\text{DM}}}{Q_{\text{DM}}} \frac{\sqrt{S_F}}{m_{\text{eff}}}} H(\omega_{\text{DM}}) \times \begin{cases} \left(\frac{\tau_{\text{DM}}}{\tau}\right)^{1/2}, & \tau \lesssim \tau_{\text{DM}} \\ \left(\frac{\tau_{\text{DM}}}{\tau}\right)^{1/4}, & \tau \gg \tau_{\text{DM}} \end{cases}. \quad (7)$$

Here,  $\Delta_{12}$  is a materially dependent suppression factor that represents the differential acceleration between the material of the membrane and that of the mirror caused by the slight difference in interaction by dark matter. For  $B - L$  (baryon-lepton) coupled dark matter,  $\Delta_{12} = \left| \frac{Z_1}{A_1} - \frac{Z_2}{A_2} \right|$ , and for  $B$  coupled dark matter,  $\Delta_{12} = \left| \frac{A_1}{\mu_1} - \frac{A_2}{\mu_2} \right|$ , where  $Z$  is the proton number,  $A$  the nucleon number,  $\mu$  the atomic mass, and the indices represent the mirror (1) and the membrane (2).  $\tau$  is the total measurement time, and  $\tau_{\text{DM}} = 2Q_{\text{DM}} / \omega_{\text{DM}}$  is the dark matter coherence time, with  $Q_{\text{DM}} = \omega_{\text{DM}} / \Delta\omega_{\text{DM}} \sim 10^6$  being the effective quality factor representing the relatively narrow linewidth of the anticipated dark matter signal, assuming ultralight dark matter ( $m_{\text{DM}} \lesssim$

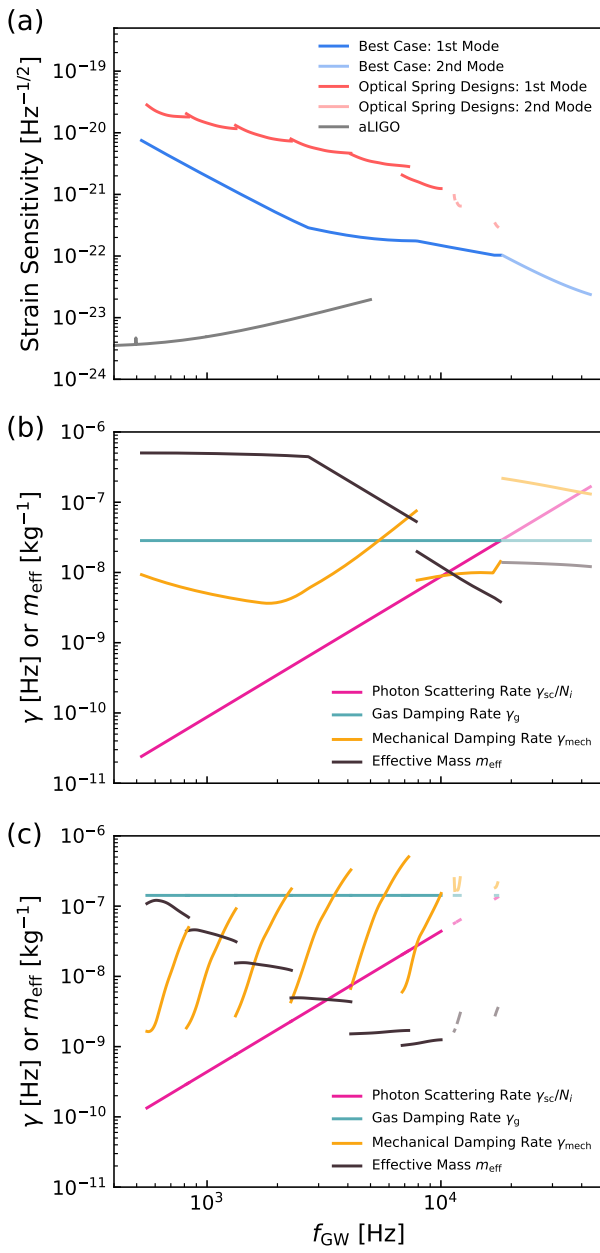


FIG. 2. a) Strain sensitivity to high frequency gravitational waves. Darker traces correspond to the s1 mode while lighter traces represent the s2 mode (see Fig. 1(b)). Blue traces represent the best case sensitivity at every resonant frequency. Red traces are six specific membrane designs, where the resonant frequency is tuned by increasing the optical trapping power from 1 to 20 W. s2 modes are shown only for the three membrane designs with the highest resonance frequencies. The aLIGO design sensitivity is shown in grey [63]. b) Damping rates contributing to Eq. 4, as well as the effective mass, for the best case scenario. Discontinuities are due to the designs yielding the best sensitivity switching from being a sweep of the lateral extent at the maximum pad size and stress to a sweep of the pad size at the maximum lateral extent and stress. c) Same as b) but for the six specific tuned membrane designs.

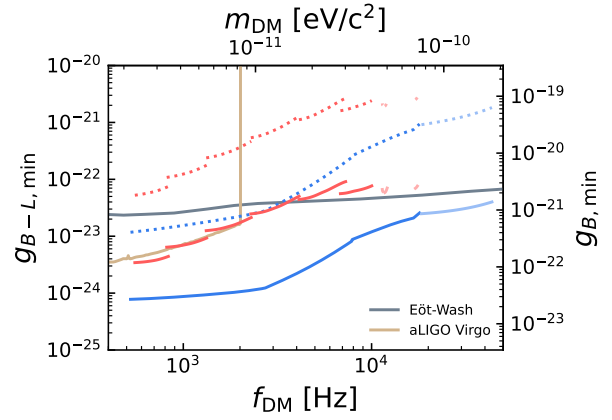


FIG. 3. Shows the sensitivity at the membrane's resonance frequency to different  $B - L$  coupled and  $B$  coupled dark matter masses of the best-case scenario membranes (blue) and the same six optically-tuned membrane designs as in Figure 2a (red). The dotted lines correspond to a measurement time of  $\tau = \tau_{DM}$  while solid lines correspond to  $\tau = 1$  year. Darker lines represent the s1 mode, while lighter lines correspond to the s2 mode [see Fig. 1]. Existing limits are shown [64], which are from aLIGO and Virgo [34] and the Eöt-Wash experiment [33].

1 eV/c<sup>2</sup>).  $\beta = \left( \iint \frac{u(x,y)}{\max[u(x,y)]} dA \right) / \left( \iint \frac{u^2(x,y)}{\max[u(x,y)]} dA \right)$  is a spatial overlap factor of a membrane mode with an assumed VDM field.  $a_0 = 3.7 \times 10^{-11} \text{ m/s}^2$  is a constant characterizing the magnitude of the acceleration caused by dark matter on a nucleon.

TABLE II. Proton number,  $Z$ , nucleon number,  $A$ , and the atomic mass,  $\mu$ , of the membrane and cavity input mirror materials used in the calculations of  $\Delta_{12}$ .

	$Z$	$A$	$\mu$ [65]	Abundance [66]
Si	14	28	27.9769265	0.92255
	29	28.9764947	0.04672	
	30	29.9737701	0.03073	
Ga	31	69	68.9255735	0.60108
	71	70	70.9247026	0.39892
As	33	75	74.9215946	1.00000

For our simulations, we use the same membrane designs and parameters as for the gravitational wave sections with a Si membrane and GaAs-based mirror, with atomic parameters summarized in Table II.

Figure 3 shows the results of the sensitivity of the best-case scenario (Sec. II D) (blue) and six optically-trapped membranes (Sec. II E) (red) to different dark matter masses in the case of  $B - L$  and  $B$  coupled dark matter. We consider both a measuring time of  $\tau = \tau_{DM}$  (dotted lines) as well as  $\tau = 1$  year (solid lines). Dark colours correspond to the s1 mode while lighter colours correspond to the s2 mode.

## V. DISCUSSION

We have presented an optomechanical platform for detecting high-frequency gravitational waves and ultralight vector dark matter across the range 0.5–40 kHz, corresponding to masses  $2 \times 10^{-12}$  to  $2 \times 10^{-10}$  eV/c<sup>2</sup>. The detector consists of two Fabry–Perot cavities in a Michelson configuration, each incorporating a nanomechanical membrane. By employing six membranes with distinct intrinsic resonance frequencies and using an optical spring generated by up to 20 W of laser power, the entire target frequency range can be covered.

The predicted sensitivity to gravitational waves, such as those potentially produced by axion superradiance [7], is comparable to that of a complementary proposal using optically levitated nanodisks in their overlapping 10–40 kHz band [20]. Optically trapped membranes provide two notable advantages over levitated nanodisks: straightforward integration within a cavity and compatibility with substantially smaller cavity end mirrors (radius  $\sim 0.2$  m, typical of LIGO) rather than the  $\sim 1$  m mirrors required by the nanodisk proposal.

For vector dark matter, the projected sensitivity of the considered best case scenario surpasses that of the Eöt-Wash experiment and that of LIGO / Virgo over  $2 \times 10^{-12}$  to  $2 \times 10^{-10}$  eV/c<sup>2</sup> for a one-year integration time, thereby extending existing experimental constraints and opening a promising window for physics beyond the Standard Model.

Future work will aim to extend the accessible frequency range to several hundred kilohertz using alternative membrane designs, such as phononic-crystal mem-

branes [27, 49]. Achieving optical tuning of a similar factor as demonstrated here for trampoline membranes (between 1.5 to 1.9), will require a much stronger optical trap. Strategies to increase the trap strength include enhancing membrane reflectivity via integrated photonic crystals [67–70] and exploiting membrane-mediated anti-crossings between optical cavity modes [71, 72]. Another promising approach is to place the membrane at a node rather than an antinode of the trapping field, which drastically reduces impinging optical power; in this inverted potential, the mechanical frequency decreases with increasing laser power [73].

Further increasing the resonance frequency by reducing the trampoline membrane’s pad size beyond the limits demonstrated here would require impractically large and costly cavity end mirrors to achieve the necessary optical focusing and suppress scattering losses, as is also the case for the nanodisk approach. A promising route to overcome this limitation is the incorporation of a metasurface lens [74] inside the cavity. Such a lens can be fabricated on a separate membrane, thereby providing the optical focusing without introducing significant thermal noise, all while being designed to avoid any resonances in the sensitivity window.

Another promising avenue is the integration of multiple membranes inside the cavity, which can enhance optomechanical coupling [75] and enables simultaneous targeting of multiple frequencies. Finally, advanced membrane-design techniques, such as topology or Bayesian optimization, may yield further gains in sensitivity by identifying geometries tailored to maximize the considered couplings [76–78].

---

[1] B. P. Abbott, R. Abbott, T. D. Abbott, M. R. Abernathy, F. Acernese, K. Ackley, C. Adams, T. Adams, P. Addesso, R. X. Adhikari, *et al.*, Observation of gravitational waves from a binary black hole merger, *Physical review letters* **116**, 061102 (2016).

[2] M. Bailes, B. K. Berger, P. R. Brady, M. Branchesi, K. Danzmann, M. Evans, K. Holley-Bockelmann, B. Iyer, T. Kajita, S. Katsanevas, *et al.*, Gravitational-wave physics and astronomy in the 2020s and 2030s, *Nature Reviews Physics* **3**, 344 (2021).

[3] E. Capote, W. Jia, N. Aritomi, M. Nakano, V. Xu, R. Abbott, I. Abouelfettouh, R. Adhikari, A. Ananyeva, S. Apertet, *et al.*, Advanced ligo detector performance in the fourth observing run, *Physical Review D* **111**, 062002 (2025).

[4] R. Schnabel and M. Korobko, Optical sensitivities of current gravitational wave observatories at higher kHz, mhz and ghz frequencies, *Scientific Reports* **15**, 25733 (2025).

[5] M. Sieniawska and M. Bejger, Continuous gravitational waves from neutron stars: Current status and prospects, *Universe* **5**, 10.3390/universe510217 (2019).

[6] N. Aggarwal, O. D. Aguiar, A. Bauswein, G. Celli, S. Clesse, A. M. Cruise, V. Domcke, D. G. Figueroa, A. Geraci, M. Goryachev, *et al.*, Challenges and opportunities of gravitational-wave searches at mhz to ghz frequencies, *Living reviews in relativity* **24**, 4 (2021).

[7] J. R. Sprague, S. L. Larson, Z. Wang, S. Klomp, A. Laeuger, G. Winstone, N. Aggarwal, A. A. Geraci, V. Kalogera, and L. Collaboration, Simulating the galactic population of axion clouds around stellar-origin black holes: Gravitational wave signals in the 10–100 kHz band, *Physical Review D* **110**, 123025 (2024).

[8] A. Patra, L. Aiello, A. Ejlli, W. L. Griffiths, A. L. James, N. Kuntimaddi, O. Kwon, E. Schwartz, H. Vahlbruch, S. M. Vermeulen, *et al.*, Broadband limits on stochastic length fluctuations from a pair of table-top interferometers, *Physical Review Letters* **135**, 101402 (2025).

[9] A. Berlin, D. Blas, R. T. D’Agnolo, S. A. Ellis, R. Harnik, Y. Kahn, and J. Schütte-Engel, Detecting high-frequency gravitational waves with microwave cavities, *Physical Review D* **105**, 116011 (2022).

[10] L. Fischer, B. Giaccone, I. Gonin, A. Grassellino, W. Hillert, T. Khabiboulline, T. Krokotsch, G. Moortgat-Pick, A. Muhs, Y. Orlov, *et al.*, First characterisation of the mago cavity, a superconducting rf detector for kHz–mhz gravitational waves, *Classical and Quantum Gravity* **42**, 115015 (2025).

[11] V. Domcke, C. Garcia-Cely, and N. L. Rodd, Novel search

for high-frequency gravitational waves with low-mass axion haloscopes, *Physical review letters* **129**, 041101 (2022).

[12] V. Domcke, S. A. Ellis, and N. L. Rodd, Magnets are weber bar gravitational wave detectors, *Physical Review Letters* **134**, 231401 (2025).

[13] R. Capdevilla, R. Harnik, T. Kim, and T. Krokotsch, High-frequency gravitational wave detection by the bread experiment, *Physical Review D* **112**, 035031 (2025).

[14] T. Bringmann, V. Domcke, E. Fuchs, and J. Kopp, High-frequency gravitational wave detection via optical frequency modulation, *Physical Review D* **108**, L061303 (2023).

[15] C. García-Cely, L. Marsili, A. Ringwald, and A. D. Spector, Polarimetric searches for axion dark matter and high-frequency gravitational waves using optical cavities, *Physical Review D* **112**, 023031 (2025).

[16] M. Goryachev and M. E. Tobar, Gravitational wave detection with high frequency phonon trapping acoustic cavities, *Physical Review D* **90**, 102005 (2014).

[17] M. Goryachev, W. M. Campbell, I. S. Heng, S. Galliou, E. N. Ivanov, and M. E. Tobar, Rare events detected with a bulk acoustic wave high frequency gravitational wave antenna, *Physical Review Letters* **127**, 071102 (2021).

[18] V. Vadakkumbatt, M. Hirschel, J. Manley, T. Clark, S. Singh, and J. Davis, Prototype superfluid gravitational wave detector, *Physical Review D* **104**, 082001 (2021).

[19] A. Arvanitaki and A. A. Geraci, Detecting high-frequency gravitational waves with optically levitated sensors, *Phys. Rev. Lett.* **110**, 071105 (2013).

[20] N. Aggarwal, G. P. Winstone, M. Teo, M. Baryakhtar, S. L. Larson, V. Kalogera, and A. A. Geraci, Searching for new physics with a levitated-sensor-based gravitational-wave detector, *Phys. Rev. Lett.* **128**, 111101 (2022).

[21] D. Chang, K. Ni, O. Painter, and H. Kimble, Ultrahigh-q mechanical oscillators through optical trapping, *New Journal of Physics* **14**, 045002 (2012).

[22] K.-K. Ni, R. Norte, D. Wilson, J. Hood, D. Chang, O. Painter, and H. Kimble, Enhancement of mechanical q factors by optical trapping, *Physical review letters* **108**, 214302 (2012).

[23] T. J. Clark, S. Bernard, J. Ma, V. Dumont, and J. C. Sankey, Optically defined phononic crystal defect, *Physical Review Letters* **133**, 226904 (2024).

[24] S. Chakram, Y. Patil, L. Chang, and M. Vengalattore, Dissipation in ultrahigh quality factor sin membrane resonators, *Physical review letters* **112**, 127201 (2014).

[25] M. D. Chowdhury, J. Manley, C. Condos, A. Agrawal, and D. Wilson, An optomechanical accelerometer search for ultralight dark matter, *arXiv preprint arXiv:2509.12175* (2025).

[26] J. Thompson, B. Zwickl, A. Jayich, F. Marquardt, S. Girvin, and J. Harris, Strong dispersive coupling of a high-finesse cavity to a micromechanical membrane, *Nature* **452**, 72 (2008).

[27] M. Rossi, D. Mason, J. Chen, Y. Tsaturyan, and A. Schliesser, Measurement-based quantum control of mechanical motion, *Nature* **563**, 53 (2018).

[28] A. E. Nelson and J. Scholtz, Dark light, dark matter, and the misalignment mechanism, *Phys. Rev. D* **84**, 103501 (2011).

[29] P. Arias, D. Cadamuro, M. Goodsell, J. Jaeckel, J. Redondo, and A. Ringwald, Wispy cold dark matter, *Journal of Cosmology and Astroparticle Physics* **2012** (06), 013.

[30] J. Manley, M. D. Chowdhury, D. Grin, S. Singh, and D. J. Wilson, Searching for vector dark matter with an optomechanical accelerometer, *Physical review letters* **126**, 061301 (2021).

[31] P. W. Graham, D. E. Kaplan, J. Mardon, S. Rajendran, and W. A. Terrano, Dark matter direct detection with accelerometers, *Physical Review D* **93**, 075029 (2016).

[32] D. Carney, A. Hook, Z. Liu, J. M. Taylor, and Y. Zhao, Ultralight dark matter detection with mechanical quantum sensors, *New Journal of Physics* **23**, 023041 (2021).

[33] T. A. Wagner, S. Schlamminger, J. H. Gundlach, and E. G. Adelberger, Torsion-balance tests of the weak equivalence principle, *Classical and Quantum Gravity* **29**, 184002 (2012).

[34] LIGO Scientific Collaboration, Virgo Collaboration, and KAGRA Collaboration (LIGO Scientific Collaboration, Virgo Collaboration, and KAGRA Collaboration), Constraints on dark photon dark matter using data from ligo's and virgo's third observing run, *Phys. Rev. D* **105**, 063030 (2022).

[35] V. Dumont, S. Bernard, C. Reinhardt, A. Kato, M. Ruf, and J. C. Sankey, Flexure-tuned membrane-at-the-edge optomechanical system, *Optics express* **27**, 25731 (2019).

[36] A. Jayich, J. Sankey, B. Zwickl, C. Yang, J. Thompson, S. Girvin, A. Clerk, F. Marquardt, and J. Harris, Dispersive optomechanics: a membrane inside a cavity, *New Journal of Physics* **10**, 095008 (2008).

[37] G. D. Cole, W. Zhang, M. J. Martin, J. Ye, and M. Aspelmeyer, Tenfold reduction of brownian noise in high-reflectivity optical coatings, *Nature Photonics* **7**, 644 (2013).

[38] G. D. Cole, W. Zhang, B. J. Bjork, D. Follman, P. Heu, C. Deutsch, L. Sonderhouse, J. Robinson, C. Franz, A. Alexandrovski, *et al.*, High-performance near-and mid-infrared crystalline coatings, *Optica* **3**, 647 (2016).

[39] R. Singh, G. D. Cole, J. Cripe, and T. Corbitt, Stable optical trap from a single optical field utilizing birefringence, *Phys. Rev. Lett.* **117**, 213604 (2016).

[40] C. Reinhardt, T. Müller, A. Bourassa, and J. C. Sankey, Ultralow-noise sin trampoline resonators for sensing and optomechanics, *Physical Review X* **6**, 021001 (2016).

[41] R. A. Norte, J. P. Moura, and S. Gröblacher, Mechanical resonators for quantum optomechanics experiments at room temperature, *Physical review letters* **116**, 147202 (2016).

[42] M. J. Bereyhi, A. Beccari, R. Groth, S. A. Fedorov, A. Arabmoheghi, T. J. Kippenberg, and N. J. Engelsen, Hierarchical tensile structures with ultralow mechanical dissipation, *Nature Communications* **13**, 3097 (2022).

[43] COMSOL AB, COMSOL Multiphysics® v. 6.2 (2023).

[44] P. R. Saulson, Thermal noise in mechanical experiments, *Physical Review D* **42**, 2437 (1990).

[45] C. Reinhardt, H. Masalehdan, S. Croatto, A. Franke, M. B. K. Kunze, J. Schaffran, N. Sültmann, A. Lindner, and R. Schnabel, Self-calibrating gas pressure sensor with a 10-decade measurement range, *ACS Photonics* **11**, 1438 (2024), <https://doi.org/10.1021/acsphotonics.3c01488>.

[46] T. Collaboration, J. Aasi, B. Abbott, R. Abbott, T. Abbott, M. Abernathy, K. Ackley, C. Adams, T. Adams, P. Addesso, *et al.*, Advanced ligo, *Class. Quantum Gravity* **32**, 074001 (2015).

[47] T. Müller, C. Reinhardt, and J. C. Sankey, Enhanced optomechanical levitation of minimally supported di-

electrics, *Physical Review A* **91**, 053849 (2015).

[48] P.-L. Yu, T. Purdy, and C. Regal, Control of material damping in high-q membrane microresonators, *Physical review letters* **108**, 083603 (2012).

[49] Y. Tsaturyan, A. Barg, E. S. Polzik, and A. Schliesser, Ultracoherent nanomechanical resonators via soft clamping and dissipation dilution, *Nature nanotechnology* **12**, 776 (2017).

[50] F. Chill, S. Wilfert, and L. Bozyk, Cryopumping of hydrogen on stainless steel in the temperature range between 7 and 18 k, *J. Vac. Sci. Technol. A* **37**, 031601 (2019).

[51] V. Baglin, Cryopumping and vacuum systems, arXiv preprint arXiv:2006.01574 (2020).

[52] Y. Tao, P. Navaretti, R. Hauert, U. Grob, M. Poggio, and C. L. Degen, Permanent reduction of dissipation in nanomechanical si resonators by chemical surface protection, *Nanotechnology* **26**, 465501 (2015).

[53] A. Beccari, D. A. Visani, S. A. Fedorov, M. J. Breyhi, V. Boureau, N. J. Engelsen, and T. J. Kippenberg, Strained crystalline nanomechanical resonators with quality factors above 10 billion, *Nature Physics* **18**, 436 (2022).

[54] M. Asheghi, Y. Leung, S. Wong, and K. Goodson, Phonon-boundary scattering in thin silicon layers, *Applied Physics Letters* **71**, 1798 (1997).

[55] J. M. Robinson, E. Oelker, W. R. Milner, W. Zhang, T. Legero, D. G. Matei, F. Riehle, U. Sterr, and J. Ye, Crystalline optical cavity at 4 k with thermal-noise-limited instability and ultralow drift, *Optica* **6**, 240 (2019).

[56] L. G. Villanueva and S. Schmid, Evidence of surface loss as ubiquitous limiting damping mechanism in sin micro- and nanomechanical resonators, *Physical review letters* **113**, 227201 (2014).

[57] A. Beccari, D. A. Visani, S. A. Fedorov, M. J. Breyhi, V. Boureau, N. J. Engelsen, and T. J. Kippenberg, Strained crystalline nanomechanical resonators with quality factors above 10 billion, *Nature Physics* **18**, 436 (2022).

[58] C.-H. Cho, Characterization of young's modulus of silicon versus temperature using a "beam deflection" method with a four-point bending fixture, *Current Applied Physics* **9**, 538 (2009).

[59] D. Franta, A. Dubroka, C. Wang, A. Giglia, J. Vohánka, P. Franta, and I. Ohlídal, Temperature-dependent dispersion model of float zone crystalline silicon, *Applied Surface Science* **421**, 405 (2017).

[60] National Center for Biotechnology Information, Pubchem compound summary for cid 783, hydrogen (2025), accessed: 2025-07-01.

[61] H. Zhang, J. Tersoff, S. Xu, H. Chen, Q. Zhang, K. Zhang, Y. Yang, C.-S. Lee, K.-N. Tu, J. Li, and Y. Lu, Approaching the ideal elastic strain limit in silicon nanowires, *Science Advances* **2**, e1501382 (2016), <https://www.science.org/doi/pdf/10.1126/sciadv.1501382>.

[62] D. Høj, U. B. Hoff, and U. L. Andersen, Ultracoherent nanomechanical resonators based on density phononic crystal engineering, *Physical Review X* **14**, 011039 (2024).

[63] R. Sturani and S. Vitale, Unofficial sensitivity curves (asd) for aligo, kagra, virgo, voyager, cosmic explorer, and einstein telescope, <https://dcc.ligo.org/ligo-t1500293/public> (2020), LIGO Document T1500293-v13, Technical Note.

[64] C. O'Hare, cajohare/axionlimits: Axionlimits, <https://cajohare.github.io/AxionLimits/> (2020).

[65] M. Wang, W. J. Huang, F. G. Kondev, G. Audi, and S. Naimi, The ame 2020 atomic mass evaluation (ii). tables, graphs and references, *Chinese Physics C* **45**, 030003 (2021).

[66] F. Kondev, M. Wang, W. Huang, S. Naimi, and G. Audi, The nubase2020 evaluation of nuclear physics properties, *Chinese Physics C* **45**, 030001 (2021).

[67] S. Fan and J. D. Joannopoulos, Analysis of guided resonances in photonic crystal slabs, *Physical Review B* **65**, 235112 (2002).

[68] V. Lousse, W. Suh, O. Kilic, S. Kim, O. Solgaard, and S. Fan, Angular and polarization properties of a photonic crystal slab mirror, *Optics express* **12**, 1575 (2004).

[69] S. Bernard, C. Reinhardt, V. Dumont, Y.-A. Peter, and J. C. Sankey, Precision resonance tuning and design of sin photonic crystal reflectors, *Optics letters* **41**, 5624 (2016).

[70] G. Enzian, Z. Wang, A. Simonsen, J. Mathiassen, T. Vibel, Y. Tsaturyan, A. Tagantsev, A. Schliesser, and E. S. Polzik, Phononically shielded photonic-crystal mirror membranes for cavity quantum optomechanics, *Optics Express* **31**, 13040 (2023).

[71] J. C. Sankey, C. Yang, B. M. Zwickl, A. M. Jayich, and J. G. Harris, Strong and tunable nonlinear optomechanical coupling in a low-loss system, *Nature Physics* **6**, 707 (2010).

[72] T. Müller, C. Reinhardt, and J. C. Sankey, Enhanced optomechanical levitation of minimally supported dielectrics, *Physical Review A* **91**, 053849 (2015).

[73] S. Dago, J. Rieser, M. A. Ciampini, V. Mlynář, A. Kugi, M. Aspelmeyer, A. Deutschmann-Olek, and N. Kiesel, Stabilizing nanoparticles in the intensity minimum: feedback levitation on an inverted potential, *Opt. Express* **32**, 45133 (2024).

[74] M. Khorasaninejad, F. Aieta, P. Kanhaiya, M. A. Kats, P. Genevet, D. Rousso, and F. Capasso, Achromatic metasurface lens at telecommunication wavelengths, *Nano Letters* **15**, 5358 (2015), pMID: 26168329, <https://doi.org/10.1021/acs.nanolett.5b01727>.

[75] X. Yao, M. H. J. de Jong, J. Li, and S. Gröblacher, Long-range optomechanical interactions in sin membrane arrays, *Phys. Rev. X* **15**, 011014 (2025).

[76] Y. Shi, F. Wang, D. Høj, O. Sigmund, and U. L. Andersen, Topology optimization of high-performance optomechanical resonator, *Advanced Science* **n/a**, e12534 (2025).

[77] D. Høj, F. Wang, W. Gao, U. B. Hoff, O. Sigmund, and U. L. Andersen, Ultra-coherent nanomechanical resonators based on inverse design, *Nature communications* **12**, 5766 (2021).

[78] D. Shin, A. Cupertino, M. H. de Jong, P. G. Steeneken, M. A. Bessa, and R. A. Norte, Spiderweb nanomechanical resonators via bayesian optimization: inspired by nature and guided by machine learning, *Advanced Materials* **34**, 2106248 (2022).